



Time-bin entanglement built in room-temperature quantum memoryTian-Huai Yang,^{1,2} Chao-Ni Zhang,^{1,2} Jian-Peng Dou,^{1,2} Xiao-Ling Pang,^{1,2} Hang Li ^{1,2} Wen-Hao Zhou,^{1,2} Yi-Jun Chang,^{1,2} and Xian-Min Jin ^{1,2,3,*}¹*Center for Integrated Quantum Information Technologies (IQIT),**School of Physics and Astronomy and State Key Laboratory of Advanced Optical Communication Systems and Networks, Shanghai Jiao Tong University, Shanghai 200240, China*²*CAS Center for Excellence and Synergetic Innovation Center in Quantum Information and Quantum Physics, University of Science and Technology of China, Hefei, Anhui 230026, China*³*TuringQ Co., Ltd., Shanghai 200240, China*

(Received 28 October 2020; revised 7 April 2021; accepted 12 April 2021; published 1 June 2021)

Quantum memory and entanglement are both the essential resources for long-distance quantum communication. Among the schemes reported to date, time-bin encoding is widely applied due to its advantage of robustness against decoherence in optical fibers. Despite enormous progress, at present the time-bin entanglement with cold-atom-ensemble-based quantum memory has to be realized in a well-isolated environment and at ultralow temperature, and the challenges for its generation in a room-temperature regime remain due to the strong noise and decoherence induced by the atomic motion and collision. Here, we report a time-bin entanglement built in room-temperature quantum memory. We propose and experimentally demonstrate a dual-addressing scheme to eliminate the strong quantum correlation between two time bins for generation of the entangled state. By using two all-fiber integrated Mach-Zehnder interferometers, we analyze the Bell inequality on the phase and obtain a visibility enabling a violation of the Clauser-Horne-Shimony-Holt Bell inequality.

DOI: [10.1103/PhysRevA.103.062403](https://doi.org/10.1103/PhysRevA.103.062403)**I. INTRODUCTION**

The construction of long-distance quantum communication is a central theme in quantum community [1,2], and its realization, associated with the vision of quantum internet, will rely on the capacities of engineering quantum entanglement, such as quantum teleportation [3], quantum swapping [4], quantum memory [5], entanglement-based quantum key distribution [6], distributed quantum computing [7], and so on. People have managed to generate and manipulate quantum entanglement in the degrees of freedom of polarization [8,9], time bin [10], path [11], and orbital angular momentum [12,13] and find that the time-bin entanglement may dominate the task of long-distance distribution due to its robustness against decoherence in optical fibers [14–16].

In contrast to the generation of time-bin entanglement via spontaneous parametric downconversion [10], spontaneous four-wave mixing [17], nitrogen vacancy centers [18], and quantum dots [19,20], the time-bin entanglement with quantum memory [21,22] could combine the advantages of flying photon qubits with the “stationary” atomic qubits and could also function as a quantum repeater [23], which has the advantage of entanglement swapping and quantum memory.

Although a great number of experimental investigations have been made in different quantum storage protocols [24–36], the generation of time-bin entanglement with quantum memory has never been achieved in a room-temperature

regime. The long-outstanding problem originates from the strong noise and decoherence induced by the atomic thermal motion and atomic collision [37,38]. Recently, the room-temperature broadband quantum memory has been realized in an atomic ensemble via far off-resonance Duan-Lukin-Cirac-Zoller (FORD) protocol [24,39,40], where the coaxial write-read scheme efficiently suppresses the dephasing of the spin wave. In contrast to polarization or path entanglement that must be built by two quantum memory systems and equipped by active phase locking, time-bin entanglement is very compatible with the coaxial scheme and only acquires a single atomic ensemble, which greatly reduces the system complexity and will further facilitate constructing large-scale memory-enabled quantum networks.

Here, we propose and experimentally demonstrate a generation of time-bin entanglement in a broadband room-temperature quantum memory. Besides the noise and decoherence issue, we have also managed to eliminate the strong quantum correlation between the two time bins via a dual-addressing scheme, which ensures the independence of ground states during two write-read periods.

II. EXPERIMENTAL SETUP

The schematic of our dual-addressing scheme is shown in Fig. 1. Two pairs of write and read pulses arrive at the atomic ensemble with a well-defined time interval of $\Delta T = 72$ ns. For each addressing pulse pair, there exists a quantum memory process. Our quantum memory employs the FORD protocol [39,40] and the atomic energy level diagram for this

*xianmin.jin@sjtu.edu.cn

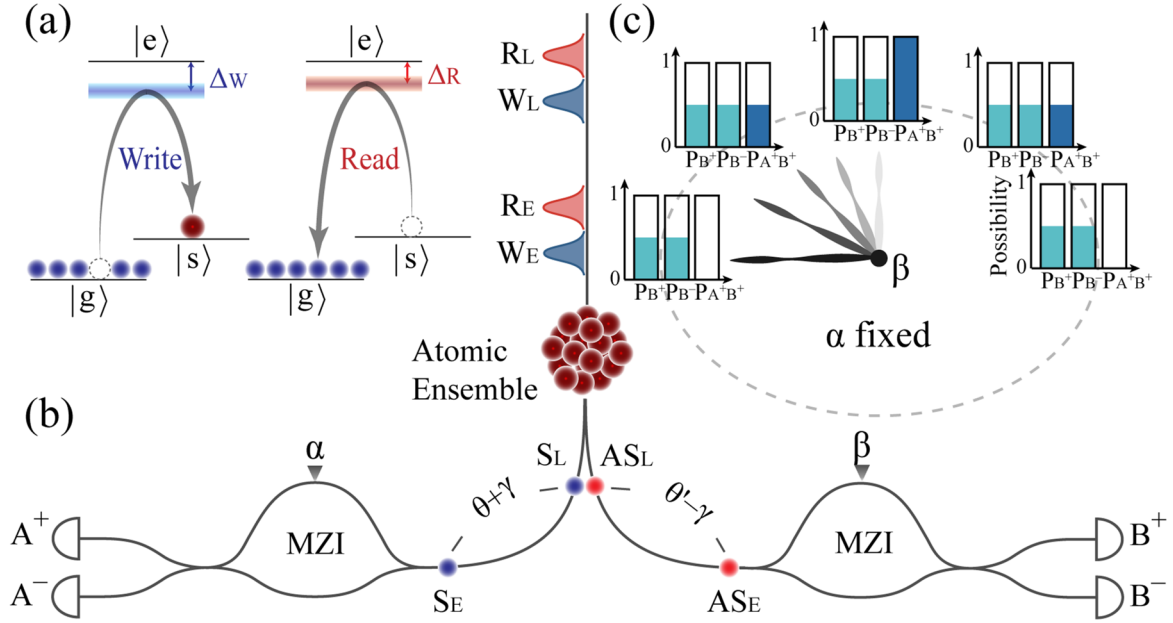


FIG. 1. The schematic diagram of the time-bin entanglement. (a) The write and read processes of the FORD protocol in a single addressing. $|g\rangle$ and $|s\rangle$ represent the hyperfine ground states and $|e\rangle$ represents the excited state. (b) The generation of time-bin entanglement in atomic ensemble with our dual-addressing scheme. W (R), the write (read) pulse; S (AS), the Stokes (anti-Stokes) photon; E (L), the early (late) time bin; MZI, unbalanced Mach-Zehnder interferometer; α (β), the phase difference in MZI. (c) The expected probability distribution of the output ports as a function of phase β , where phase α is fixed. P_{B^+} (P_{B^-}), the probability of the output port B^+ (B^-); $P_{A^+B^+}$, the coincidence probability between the output port A^+ and B^+ .

protocol is shown in Fig. 1(a). Initially, all atoms are prepared in the ground state $|g\rangle$ of ^{133}Cs by the strong pump 1, and then a write pulse with a detuning of $\Delta W = 13.2$ GHz induces a broadband Stokes photon via spontaneous Raman scattering, meanwhile heralding a collective excitation state $|s\rangle$ among the atoms. The collective excitation state can be expressed as [4]

$$\frac{1}{\sqrt{N}} \sum_{n=1}^N e^{i(\mathbf{k}_W - \mathbf{k}_S) \cdot \mathbf{r}_n} |g_1, \dots, s_n, \dots, g_N\rangle, \quad (1)$$

where N is the total number of atoms, \mathbf{k}_W is the wave vector of the write pulse, \mathbf{k}_S is the wave vector of the Stokes photon, and \mathbf{r}_n is the position of the n th atom. After a designed storage time, a read pulse with a detuning of $\Delta R = 4$ GHz retrieves the collective excitation state as a broadband anti-Stokes photon. The wave vector of the read pulse is denoted by \mathbf{k}_R and the wave vector of the anti-Stokes photon is denoted by \mathbf{k}_{AS} . The polarizations of Stokes and anti-Stokes photons are orthogonal to the control pulse [41] in the write and read process, which can be used to filter out the control pulse effectively by a Wollaston prism. The experimental setup is shown in Fig. 2 (see Appendix A for more details).

We adopt the coaxial scheme by using one laser to generate both write and read pulses [42], which can well suppress the dephasing of the spin wave meanwhile implying $\mathbf{k}_W = \mathbf{k}_R$ [43]. In other words, the write pulse can act as the read pulse to retrieve the anti-Stokes photons, and vice versa. So, it is very challenging to ensure that the early read pulse R_E exclusively retrieves the collective excitation state generated by the early write pulse W_E and that the late read pulse R_L exclusively retrieves the collective excitation state generated

by the late write pulse W_L . We therefore propose a dual-addressing scheme to solve this problem in two steps. The first step is to use pump 1 with a pump time of 300 ns, ensuring the independence between different experimental periods.

The second and most critical step is to add pump 2 between the two write and read processes. Pump 2, with a pump time of 40 ns, is resonant with the $|s\rangle \rightarrow |e\rangle$ transition. It reinitializes the ground state of the atomic ensemble and imposes a perturbation on the phase, causing the phase difference between the Stokes photons induced by the two write processes to contain two portions: one is a constant phase difference, θ , caused by the fixed identical time interval ΔT ; the other one is a variable phase difference, γ , a random phase fluctuation caused by the pump process. This characteristic induces the statistical average beam-splitting ratio of the output of Mach-Zehnder interferometers (MZIs) to be a constant of 50:50 [see Fig. 1(c)]. It can be well confirmed by the autocorrelation of the Stokes photons [44] (see Appendix D). The autocorrelation without pump 2 is $g_{S_E-S_L}^{(2)} = 1.94 \pm 0.03$, well matching the thermal noise distribution of the Stokes photons. However, the autocorrelation with a 292.8-pJ pump 2 is $g_{S_E-S_L}^{(2)} = 1.15 \pm 0.03$, indicating the independence between the two Stokes photons. As for the read process, the phase difference between the anti-Stokes photons contains a constant phase difference, θ' and a variable phase difference, $-\gamma$, which leads to the constant phase difference φ of the whole process (see Appendix E). Since the excitation rate of the write pulse is too low to simultaneously create two collective excitation states, the time-bin entangled state can be written as

$$\Psi = \frac{1}{\sqrt{2}} (|E\rangle_S |E\rangle_{AS} + e^{i\varphi} |L\rangle_S |L\rangle_{AS}), \quad (2)$$

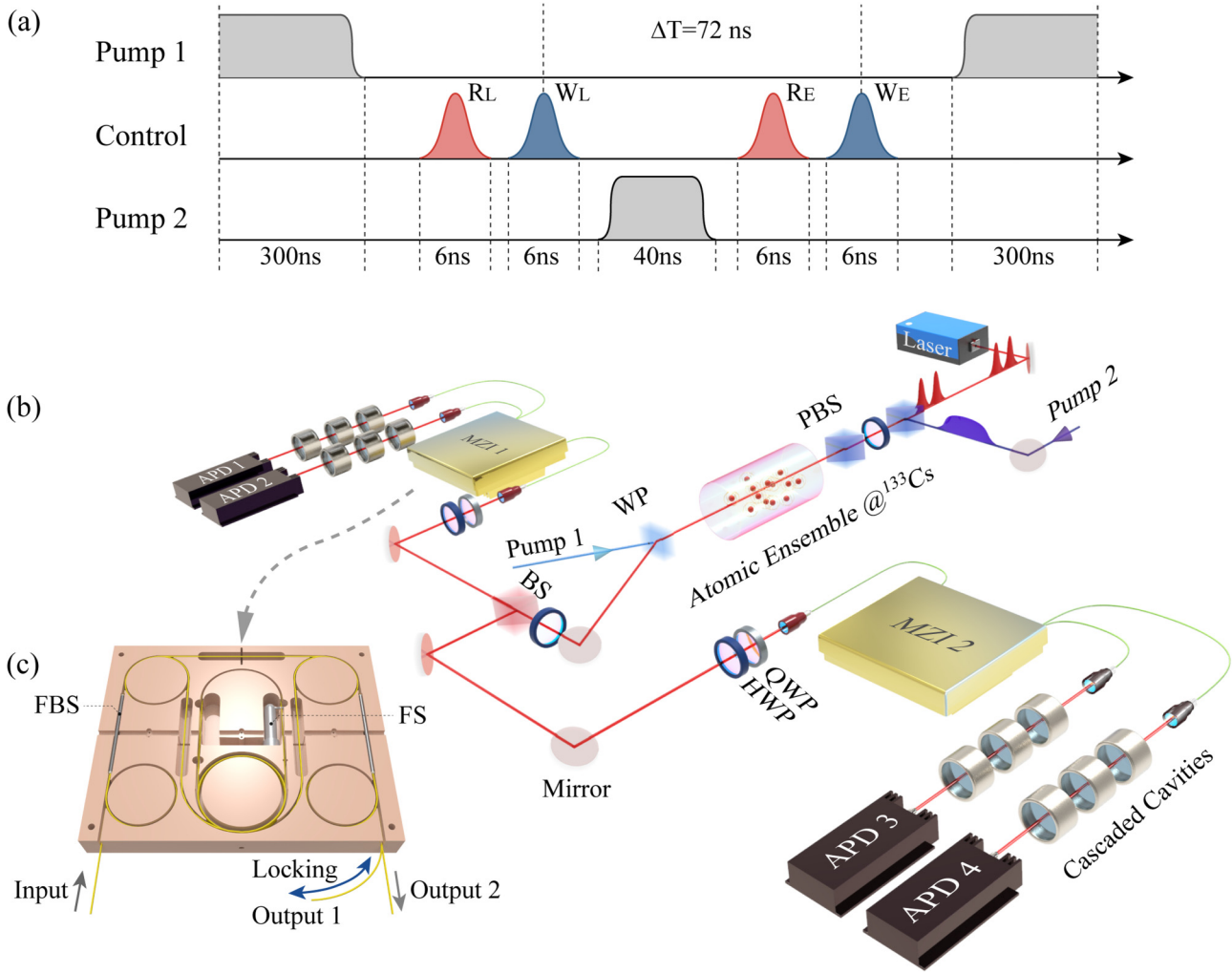


FIG. 2. Experimental setup. (a) Time sequences of the addressing pulses. (b) The control pulse with horizontal polarization and pump 2 with vertical polarization are combined on the polarization beam splitter (PBS), and then they are prepared in horizontal polarization via a half-wave plate (HWP) and another PBS. Pump 1 with horizontal polarization is overlapped with the control pulse in a counterpropagating configuration. Since the signal photons (Stokes and anti-Stokes photons) are in vertical polarization, a Wollaston prism (WP) after atomic ensemble can filter out the control light efficiently. With a beam splitter (BS), the signal photons are separated into two identical MZIs for Bell inequality measurement. Two cascaded Fabry-Perot cavities with central frequency of the Stokes photon or the anti-Stokes photon can contribute to a total extinction ratio of $10^7 : 1$. QWP, quarter-wave plate; APD, avalanche photodiode. (c) The photo of our homemade device of MZI. FBS, fiber beam splitter; FS, fiber stretcher.

where $|E\rangle$ or $|L\rangle$ represents a photon generated by the early pulse or the late pulse, respectively. The indexes S and AS represent Stokes and anti-Stokes photons, respectively.

III. RESULTS OF TIME-BIN ENTANGLEMENT

To directly analyze the performance of pump 2, we measure the cross-correlation $g_{S_i-AS_j}^{(2)}$ between the Stokes photons and the anti-Stokes photons from different addressing processes. The experimental result is shown in Fig. 3(a) as a function of the pump power. Cross-correlation of the early process $g_{S_E-AS_E}^{(2)}$ is a constant by theory. As for cross-correlation of the late process $g_{S_L-AS_L}^{(2)}$, the value rises to a maximum rapidly, for the reason of sharply decreasing noise counts of the unwanted anti-Stokes photons N_{AS_L} , which are

generated by the late read pulse, as shown by the red squares in Fig. 3(b). It also reasonably explains the result of the gently decreasing value $g_{S_L-AS_L}^{(2)}$ after the maximum, for the noise increasing. As the value of the cross-correlation $g_{S_L-AS_L}^{(2)}$ approaches the cross-correlation $g_{S_E-AS_E}^{(2)}$, this shows that the two processes have a similar but independent performance. Moreover, according to the Cauchy-Schwarz inequality [45] $(g_{S-AS}^{(2)})^2 \leq g_{S-S}^{(2)}g_{AS-AS}^{(2)}$, the cross-correlation $g_{S-AS}^{(2)} \geq 2$ enables a violation given the fact that autocorrelation is always less than 2. In our system, cross-correlations obtained in both the early process and the late one are always over 15, indicating nonclassical correlation of the photons.

To further investigate the independence between the two addressing processes, we also measure the correlation between the early write pulse and late read pulse. As is shown in Fig. 3, the cross-correlation $g_{S_E-AS_L}^{(2)}$ and the coincidence

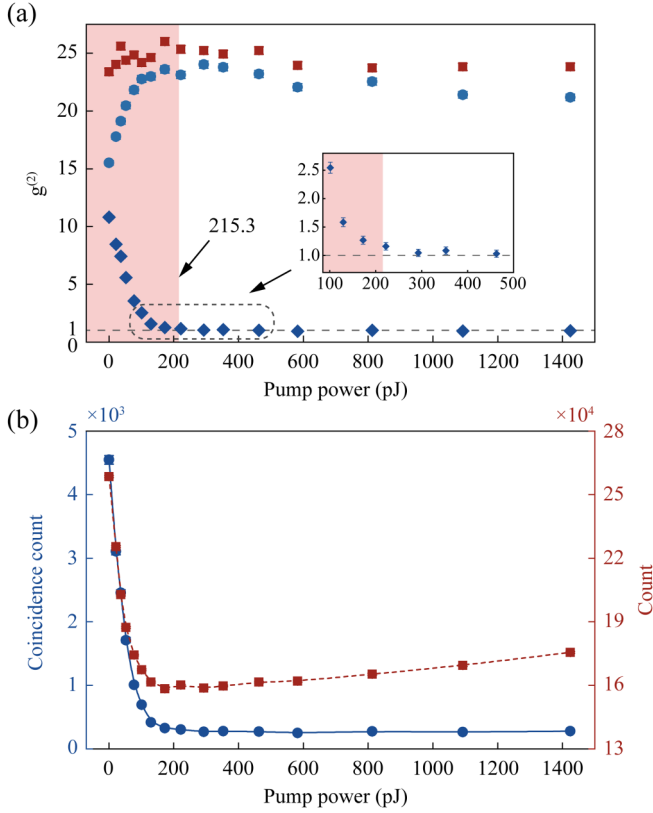


FIG. 3. Performance of the write and read process. (a) The cross-correlation of the Stokes photons and the anti-Stokes photons vary as a function of the power of pump 2. Red square, the cross-correlation of the early process $g_{SE-ASE}^{(2)}$; light blue circle, the cross-correlation of the late process $g_{SL-ASL}^{(2)}$; dark blue diamond, the cross-correlation of the early write pulse and the late read pulse $g_{SE-ASL}^{(2)}$. The inset is the partial enlarged view of the dotted frame. (b) The experimental counts vary as a function of the power of pump 2. Dark blue circles refer to the coincidence counts N_{SE-ASL} and red squares refer to the anti-Stokes photon counts N_{ASL} . Error bars are too small to be recognized and are given by Poissonian statistics.

count N_{SE-ASL} have a similar trend. The value of the cross-correlation drops sharply and stabilizes at 1, which represents the unrelated random coincidence. This shows that it is impossible for the late read pulse to retrieve the collective excitation state generated by the early write pulse. There exists an optimum point of the performance of pump 2, and we select the pump power of 215.3 pJ in the following experiment as the dividing line shown in Fig. 3(a).

The quantum state built in room-temperature quantum memory can be verified by using two MZIs with Franson interference [46]. In contrast to previous demonstrations [14,21], it is a great challenge to adjust while maintaining the phase with the heavily unbalanced arm and the low locking laser power of 50 μ W in our experiment. In practice, we simultaneously apply a passive stabilization by locking the temperature to reduce the environmental disturbance. Moreover, to better regulate the phase for Bell inequality measurement, we implant an optical fiber stretcher in the long arm with a feedback to strictly lock the phase at a specific value on demand (see Appendix B for more details).

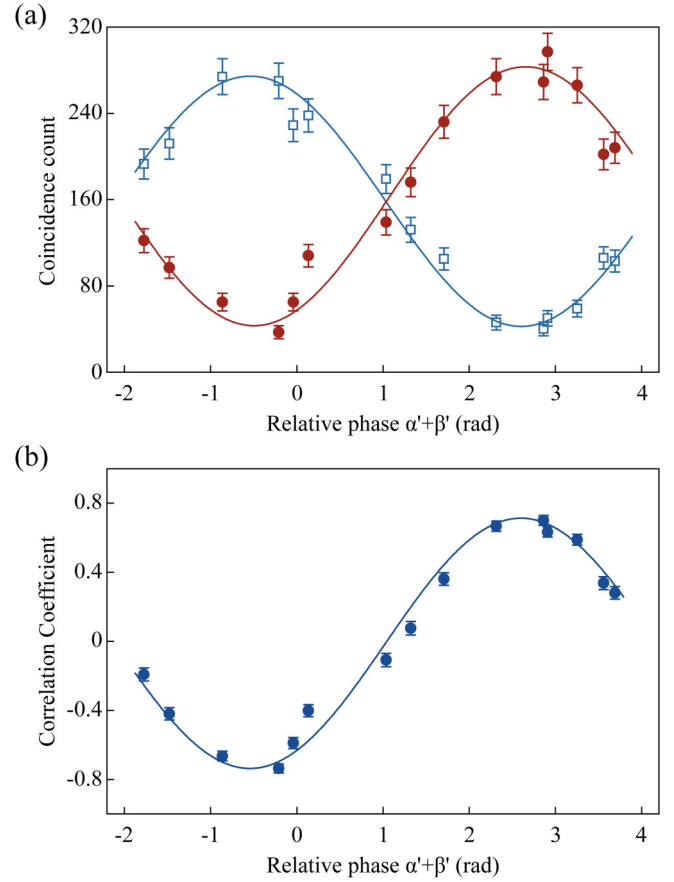


FIG. 4. Characterization of two-photon interference. (a) Coincidence count between the detectors A^+B^+ (blue hollow squares) and A^+B^- (red dot) vary as a function of the phase of $\alpha' + \beta'$. (b) Measured correlation coefficient E varies as a function of the phase of $\alpha' + \beta'$. Error bars are given by Poissonian statistics.

Each detector can catch three count peaks in a time sequence. The first peak refers to photons generated by the early pulse going through the short arm of the MZIs. The third peak refers to photons generated by the late pulse going through the long arm. The second peak refers to photons generated by the early pulse going through the long arm or photons generated by the late pulse going through the short arm. Only the second peak is used for the phase projection and the Bell inequality measurement. The quantum state projecting to the detector A^+ in the second peak can be written as $\phi_{A^+} = \frac{1}{\sqrt{2}}[e^{i\alpha} + e^{i(\theta+\gamma)}]|A^+\rangle$, and the coincidence event probability between the detector A^i and B^j is $P_{A^iB^j} = \frac{1}{2} + \frac{1}{2}ijV \cos(\alpha' + \beta')$, where i and $j = \pm 1$, V is the visibility of interference fringes, and $\alpha' = \alpha - \theta$ and $\beta' = \beta - \theta'$ are the relative phases (see Appendix F for more details). In Fig. 4(a), we show the coincidence count as a function of the phase $\alpha' + \beta'$, where we fix the phase α' and scan the phase β' . Furthermore, in Fig. 4(b), we show the correlation coefficient E inferred by the probability as $E = (\sum_{ij} ijP_{A^iB^j}) / (\sum_{ij} P_{A^i}P_{B^j})$, and we obtain the two-photon interference fringes with the visibility of $V = 0.74 \pm 0.02$, which is above the threshold required for the Clauser-Horne-Shimony-Holt Bell inequality violation ($V \geq 1/\sqrt{2}$) [47].

IV. CONCLUSION

In summary, we present an experimental generation of time-bin entanglement in a broadband room-temperature quantum memory. Our experiment, along with the programmable storage time, may serve as a crucial element in future environmentally friendly quantum repeaters. In combination with quantum frequency conversion to telecommunication band [48–50], our work may help to construct a quantum network with capacities of both local buffer and long-distance quantum connection, supporting quantum teleportation, entanglement-based quantum key distribution, and distributed quantum computing.

ACKNOWLEDGMENTS

The authors thank Jian-Wei Pan for helpful discussions. This research is supported by the National Key R&D Program of China (Grants No. 2019YFA0308700, No. 2019YFA0706302, and No. 2017YFA0303700); National Natural Science Foundation of China (NSFC) (Grants No. 11904229, No. 61734005, No. 11761141014, and No. 11690033); Science and Technology Commission of Shanghai Municipality (STCSM) (Grants No. 20JC1416300 and No. 2019SHZDZX01); Shanghai Municipal Education Commission (SMEC) (Grant No. 2017-01-07-00-02-E00049); China Postdoctoral Science Foundation (Grant No. 2020M671091). X.-M.J. acknowledges support from Zhiyuan Innovative Research Center of Shanghai Jiao Tong University and additional support from a Shanghai talent program.

APPENDIX A: EXPERIMENTAL DETAILS

We select the cesium atoms ^{133}Cs as our atomic ensemble and place them in a 75-mm-long cell with 10 Torr Ne buffer gas. The cesium cell is packed in a magnetic shielding and heated up to 61 °C for a large optical depth. In our system, the frequency of the pump light (both pump 1 and pump 2) is locked to the transition $6S_{1/2}, F = 4$, to $6S_{3/2}, F' = 4$ to 5, line of ^{133}Cs . To be specific, pump 1 is 300 ns generated by an acousto-optic modulator with an extinction ratio of 17 500:1 and the power of 24 mW. Since the write pulse and the read pulse share the same laser, both of them have a 4-GHz detuning with the frequency of the pump light. So, the Stokes photon, the anti-Stokes photon, the write pulse, the read pulse, and the pump light at least exist a frequency difference of 4 GHz between each other. Via two cascaded Fabry-PÉrot cavities, whose central frequency is that of the Stokes photon or the anti-Stokes photon and whose transmission window full width at half maximum is about 380 MHz, these photons with different frequencies can be separated and filtered efficiently. The total extinction ratio reaches $10^7:1$.

APPENDIX B: PERFORMANCE OF MZI

The experimental setup of the all-fiber integrated Mach-Zehnder interferometer is shown in Fig. 2(c), which has a large path difference of 14.4 m. For each interferometer, all devices are stuck in an aluminum alloy mold and made of polarization maintaining optical fiber. In order to have the same frequency drifting between locking light and the photons

induced by control light, we make use of the same laser to generate the locking light and the control light. The frequency difference between locking light and signal photons is so small that we cannot separate them by a dichroic mirror. In practice, we use a Glan-Taylor prism to separate the locking light and signal photons via the different polarization. To reduce the noise from the locking light, the signal photons with horizontal polarization inject the MZI from one input port, but the continuous locking light with vertical polarization reversely injects the MZI from output 1 and is detected by a photoelectric amplifier in the other input port. Moreover, the thermal expansion coefficient of the fiber is around $5 \times 10^{-7}/^\circ\text{C}$, so we combine three thermoelectric coolers with a proportional-integral-derivative control to maintain the interferometer with a laboratory temperature of 20 °C. To better adjust and control the phase, we arrange an optical fiber stretcher at the long arm, which would actively feed back according to the interference results of the locking light.

To clearly obtain the visibility of the MZI, initially, we lock the phase in a position of maximum interference intensity, and then we swiftly flip the phase of π , where the interference intensity is minimum. Finally, we obtain the interference intensity as a function of time by an oscilloscope. The performance of the two MZIs is shown in the Fig. 5, and the visibility can be inferred by

$$V = \frac{\bar{I}_{\text{Max}} - \bar{I}_{\text{Min}}}{\bar{I}_{\text{Max}} + \bar{I}_{\text{Min}}}, \quad (\text{B1})$$

where \bar{I}_{Max} represents the average value of the maximum interference intensity and \bar{I}_{Min} represents the average value of the minimum interference intensity. The visibility of two MZIs is 97.15% and 96.38%, respectively.

Compared with the free-space MZI, our all-fiber integrated MZI has the advantages of temperature stability and compactness, which makes the interference performance more stable.

In our work, the active stabilization is realized by the means of the fiber stretcher. Its function is to compensate the path change caused by the environment to maintain the stability of the interferometer. The maximum modulation frequency of the fiber stretcher is 30 KHz; however, the impact caused by the environment is a slow change. So we set the modulation frequency of the fiber stretcher to 2 KHz. In the experiment, the interferometer is a device of the quantum entanglement analysis, which does not need to be adjusted all the time. Thus, the fiber stretcher does not affect the quantum memory bandwidth. In addition, the operating wavelength of the polarization maintaining fiber is 770 to 1100 nm, and the bandwidth of our signal photons is about 380 MHz at 852 nm. So the effect of polarization maintaining fiber on bandwidth can be ignored and the broadband signal photons generated by our system can pass through the interferometer unaffectedly.

APPENDIX C: IMPROVEMENT OF VISIBILITY

In our work, there are two main factors that affect the visibility, one is the performance of the quantum memory and the other is the visibility of the interferometer itself. So, we can enhance the visibility in the following ways:

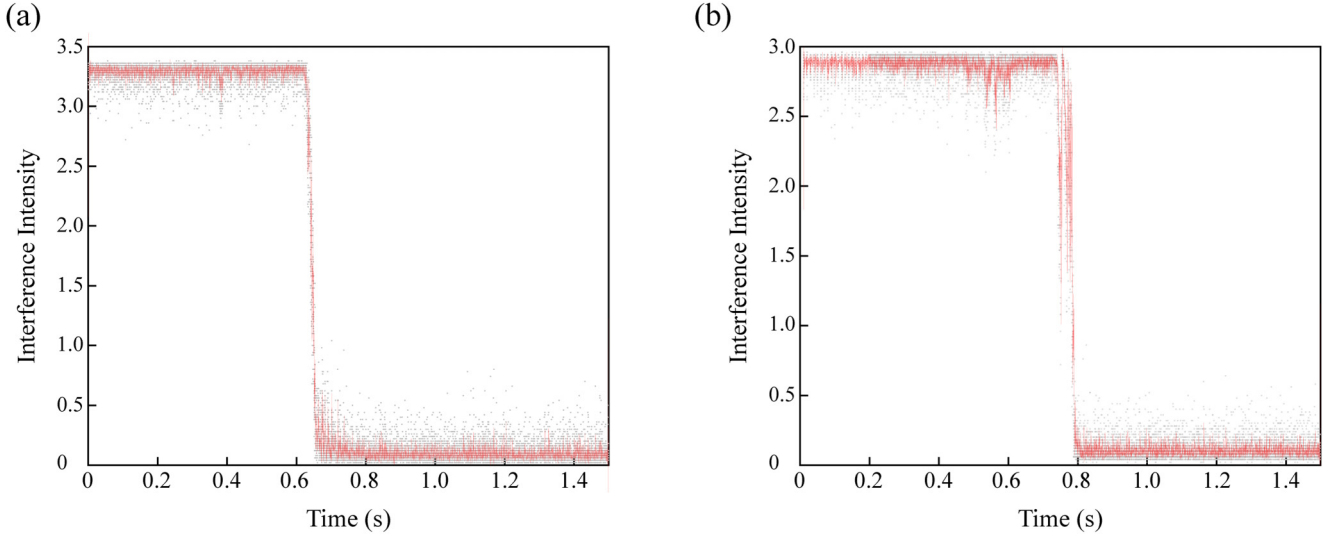


FIG. 5. Performance of the two MZIs. The interference intensity of MZI 1 (a) and MZI 2 (b) varies as a function of time.

First, the relationship between the intensity cross-correlation and the maximum ideal visibility is shown as

$$V = \frac{g_{S-AS}^{(2)} - 1}{g_{S-AS}^{(2)} + 1}, \quad (\text{C1})$$

where V represents the maximum ideal visibility and $g_{S-AS}^{(2)}$ represents the cross-correlation between the Stokes photon and the anti-Stokes photon. Thus, we can enhance the intensity cross-correlation by reducing the experimental background noise and optimizing the write and read pulses with the power and beam waist radius [43].

Second, the structure diagram of the MZI is shown in the Fig. 6. FBS is the fiber beam splitter. In general, the transmittance of flange is about 85% and the optical fiber transmission loss is 4 dB/km of our signal wavelength. Thus, the channel loss between the long arm and the short arm is unequal. The different channel loss between the two arms mainly comes from the different numbers of flanges in the two arms. Thus, the flange can be removed by applying optical fiber fusion splicing. In addition, a FBS with a special beam-splitting ratio can be employed as the FBS1 to enhance the visibility of the interferometer itself.

APPENDIX D: AUTOCORRELATION FUNCTION

In our work, the time sequence of the autocorrelation function measurement is shown in Fig. 7. Initially, all atoms are prepared in the ground state $|g\rangle$ by a strong pump, and then

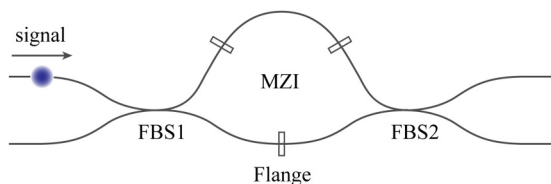


FIG. 6. Structure diagram of the MZI.

two write pulses arrive at the atomic ensemble with a time interval. As two write processes (W_0 and W_1) are independent, each pulse has a certain probability ε_1 to induce a broadband Stokes photon via spontaneous Raman scattering, and the state can be written as

$$\psi = \varepsilon_0|0\rangle_0|0\rangle_1 + \sqrt{\varepsilon_1}|1\rangle_0|0\rangle_1 + \sqrt{\varepsilon_1}|0\rangle_0|1\rangle_1 + \varepsilon_1|1\rangle_0|1\rangle_1, \quad (\text{D1})$$

where $|0\rangle$ or $|1\rangle$ represents the number of Stokes photons, respectively. Index 0 or 1 represents time t_0 or time t_1 , respectively. ε_0 represents the probability of no collective excitation state induced by the write pulse. ε_1 represents the excitation rate of the write pulse.

As shown in Ref. [44], the autocorrelation function can be written as

$$g^{(2)}(\tau) = \frac{\langle a_1^+ a_0^+ a_0 a_1 \rangle}{\langle a_0^+ a_0 \rangle \langle a_1^+ a_1 \rangle}. \quad (\text{D2})$$

Making use of Eq. (D1), the autocorrelation function is given as

$$g^{(2)}(\tau) = \frac{\varepsilon_1^2}{(\varepsilon_1 + \varepsilon_1^2)^2} = \frac{1}{1 + 2\varepsilon_1 + \varepsilon_1^2}. \quad (\text{D3})$$

In our work, the excitation rate ε_1 is about 0.6%, far less than 1, so the autocorrelation $g^{(2)}(\tau) \approx 1$ represents the independent correlation between the two write processes (W_0 and W_1).

APPENDIX E: THEORETICAL DERIVATION OF TIME-BIN ENTANGLEMENT GENERATION

We first consider the FORD quantum memory scheme with only one write and read process. As we do not consider higher-order excitation, the state of the write process can be written as

$$\psi_W = \sqrt{1 - \eta_1}|0_c 0_s\rangle + \sqrt{\eta_1} e^{i(\varphi_c + \varphi_s)} |1_c 1_s\rangle, \quad (\text{E1})$$

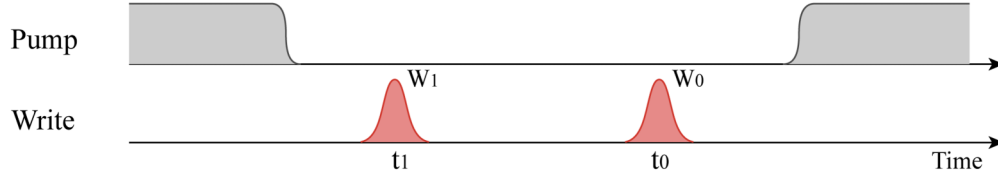


FIG. 7. Time sequences of the autocorrelation function measurement.

where the index “c” represents the atomic spin wave, the index “s” represents the Stokes field, and η_1 represents the excitation rate. So, the state of the read process can be written as

$$\psi_R = \sqrt{1 - \eta_2} |0_s 0_{as}\rangle + \sqrt{\eta_2} e^{i(\varphi_s + \varphi_{as})} |1_s 1_{as}\rangle, \quad (\text{E2})$$

where the index “as” represents the anti-Stokes field and η_2 represents the total retrieval efficiency of the quantum memory. Now we consider the time-bin entanglement in our work. The state of two write and read processes can be written as

$$\begin{aligned} \psi &= \psi_E \otimes \psi_L \\ &= \sqrt{1 - 2\eta_2 - \eta_2^2} |0_s 0_{as}\rangle_E |0_s 0_{as}\rangle_L \\ &\quad + \sqrt{\eta_2} e^{i(\varphi_s + \varphi_{as})_E} |1_s 1_{as}\rangle_E |0_s 0_{as}\rangle_L \\ &\quad + \sqrt{\eta_2} e^{i(\varphi_s + \varphi_{as})_L} |0_s 0_{as}\rangle_E |1_s 1_{as}\rangle_L \\ &\quad + \eta_2 e^{i[(\varphi_s + \varphi_{as})_E + (\varphi_s + \varphi_{as})_L]} |1_s 1_{as}\rangle_E |1_s 1_{as}\rangle_L. \end{aligned} \quad (\text{E3})$$

If only one Stokes photon is detected, the time-bin entangled state gives

$$\begin{aligned} \Psi &= \frac{1}{\sqrt{2}} e^{i(\varphi_s + \varphi_{as})_E} |E\rangle_S |E\rangle_{AS} \\ &\quad + \frac{1}{\sqrt{2}} e^{i(\varphi_s + \varphi_{as})_L} |L\rangle_S |L\rangle_{AS}, \end{aligned} \quad (\text{E4})$$

where $|E\rangle$ or $|L\rangle$ represents a photon generated by the early pulse or the late pulse, respectively. The indexes S and AS represent Stokes and anti-Stokes photons, respectively. For the phase of Stokes photon φ_s , it consists of the initial Stokes field φ_{s0} and the path phase φ_{sp} . Thus, for the Stokes photons produced by the early pulse or the late pulse, their phases can be written as

$$\varphi_{sE} = \varphi_{s0E} + \varphi_{spE}, \quad (\text{E5})$$

$$\varphi_{sL} = \varphi_{s0L} + \varphi_{spL}. \quad (\text{E6})$$

For the anti-Stokes photons produced by the early pulse or the late pulse, their phases can be written as

$$\varphi_{asE} = \varphi_{as0E} + \varphi_{aspE}, \quad (\text{E7})$$

$$\varphi_{asL} = \varphi_{as0L} + \varphi_{aspL}. \quad (\text{E8})$$

So, Eq. (E4) can be written as

$$\begin{aligned} \Psi &= \frac{1}{\sqrt{2}} (e^{i(\varphi_s + \varphi_{as})_E} |E\rangle_S |E\rangle_{AS} + e^{i(\varphi_s + \varphi_{as})_L} |L\rangle_S |L\rangle_{AS}) \\ &= \frac{1}{\sqrt{2}} (|E\rangle_S |E\rangle_{AS} + e^{i(\Delta\varphi_{s0} + \Delta\varphi_{as0} + \Delta\varphi_{sp} + \Delta\varphi_{asp})} |L\rangle_S |L\rangle_{AS}), \end{aligned} \quad (\text{E9})$$

where

$$\Delta\varphi_{s0} = \varphi_{s0L} - \varphi_{s0E}, \quad (\text{E10})$$

$$\Delta\varphi_{as0} = \varphi_{as0L} - \varphi_{as0E}, \quad (\text{E11})$$

$$\Delta\varphi_{sp} = \varphi_{spL} - \varphi_{spE}, \quad (\text{E12})$$

$$\Delta\varphi_{asp} = \varphi_{aspL} - \varphi_{aspE}. \quad (\text{E13})$$

Since the phase between the atomic spin wave and the Stokes field is anticorrelation [51,52], we have

$$\varphi_W = \varphi_s + \varphi_c, \quad (\text{E14})$$

$$\varphi_{as0} = \pi + \varphi_c + \varphi_R, \quad (\text{E15})$$

where φ_W is the phase of the write pulse and φ_R is the phase of the read pulse. So, we have

$$\begin{aligned} \Delta\varphi_{as0} &= (\varphi_c + \varphi_R)_L - (\varphi_c + \varphi_R)_E \\ &= \Delta\varphi_R + (\varphi_{cL} - \varphi_{cE}) \\ &= \Delta\varphi_R + \Delta\varphi_W - \Delta\varphi_{s0}. \end{aligned} \quad (\text{E16})$$

Therefore, Eq. (E9) can be written as

$$\Psi = \frac{1}{\sqrt{2}} (|E\rangle_S |E\rangle_{AS} + e^{i\varphi} |L\rangle_S |L\rangle_{AS}), \quad (\text{E17})$$

where

$$\varphi = \Delta\varphi_R + \Delta\varphi_W + \Delta\varphi_{sp} + \Delta\varphi_{asp} = \text{const.} \quad (\text{E18})$$

Thus, the constant phase difference mentioned above is the phase φ , and the variable phase difference γ is the random phase difference of the initial Stokes field $\Delta\varphi_{s0}$.

APPENDIX F: BELL INEQUALITY ON PHASE PROJECTION

As mentioned above, the state of Stokes photons before injecting the MZI can be written as

$$\psi_A = \frac{1}{\sqrt{2}} (|E\rangle_S + e^{i(\theta + \gamma)} |L\rangle_S), \quad (\text{F1})$$

where the constant phase difference $\theta = \Delta\varphi_{sp}$ is the phase difference of the path. The variable phase difference γ is the phase difference of the initial Stokes field $\Delta\varphi_{s0}$. So, the state of anti-Stokes photons before injecting the MZI can be written as

$$\psi_B = \frac{1}{\sqrt{2}} (|E\rangle_{AS} + e^{i(\theta' - \gamma)} |L\rangle_{AS}), \quad (\text{F2})$$

where the constant phase difference $\theta' = \Delta\varphi_W + \Delta\varphi_R + \Delta\varphi_{asp}$ is the sum of the phase difference of the write pulse $\Delta\varphi_W$, the phase difference of the read pulse $\Delta\varphi_R$, and the phase difference of the path $\Delta\varphi_{asp}$.

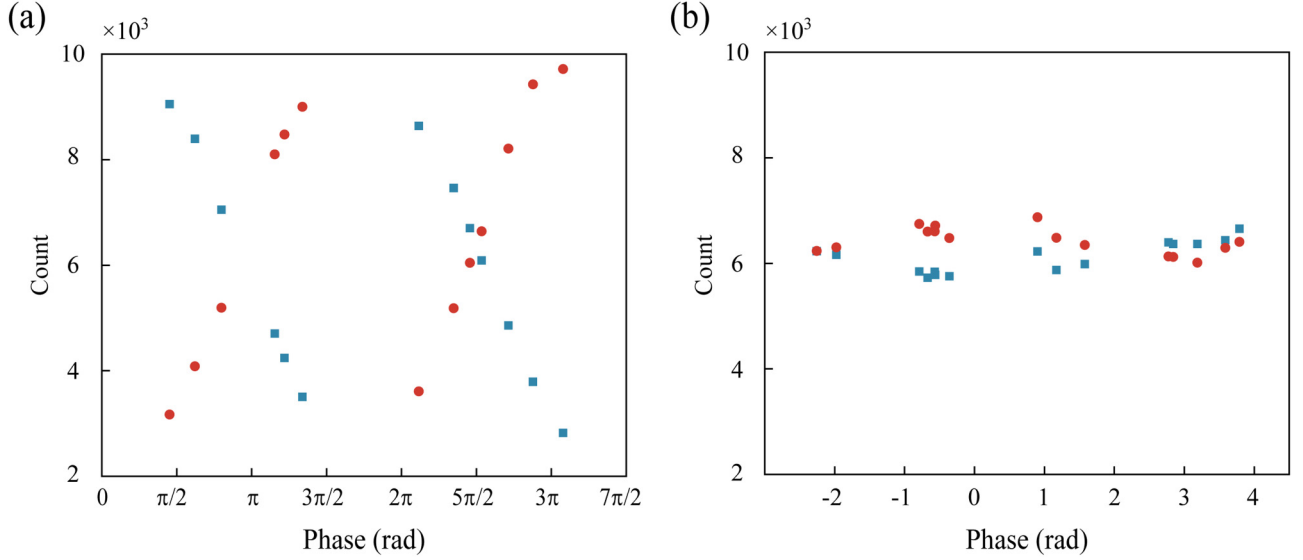


FIG. 8. Effect of pump 2. The experimental counts vary as the function of the phase, without pump 2 (a) or with pump 2 (b). Blue squares, the counts of the output port B^+ ; red circles, the counts of the output port B^- .

For each output of the MZI, there are three count peaks. If we only consider the second count peak, the state of the Stokes photon can be written as

$$\begin{aligned} \psi'_A = & \frac{1}{2}(e^{i\alpha'}|A^+\rangle_E + e^{i(\alpha'+\pi/2)}|A^-\rangle_E) \\ & + \frac{1}{2}(e^{i(\gamma+\pi/2)}|A^+\rangle_L + e^{i\gamma}|A^-\rangle_L), \end{aligned} \quad (\text{F3})$$

The anti-Stokes photon has a similar state written as

$$\begin{aligned} \psi'_B = & \frac{1}{2}(e^{i\beta'}|B^+\rangle_E + e^{i(\beta'+\pi/2)}|B^-\rangle_E) \\ & + \frac{1}{2}(e^{i(-\gamma+\pi/2)}|B^+\rangle_L + e^{-i\gamma}|B^-\rangle_L), \end{aligned} \quad (\text{F4})$$

Making use of Eq. (2), the normalized coincidence state gives

$$\begin{aligned} \psi_{AB} = & \frac{1}{2\sqrt{2}}(e^{i(\alpha'+\beta')}|A^+B^+\rangle + e^{i(\alpha'+\beta'+\pi/2)}|A^+B^-\rangle \\ & + e^{i(\alpha'+\beta'+\pi/2)}|A^-B^+\rangle + e^{i(\alpha'+\beta'+\pi)}|A^-B^-\rangle) \\ & + \frac{1}{2\sqrt{2}}(e^{i\pi}|A^+B^+\rangle + e^{i\pi/2}|A^+B^-\rangle \\ & + e^{i\pi/2}|A^-B^+\rangle + |A^-B^-\rangle), \end{aligned} \quad (\text{F5})$$

where α' and β' are the relative phases. The first part of Eqs. (F3)–(F5) is contributed by the early photons going through the long arm of the MZI, and the second part is contributed by the late photons going through the short arm. Equation (F5) shows that the random phase γ cannot affect the coincidence measurement between Stokes and anti-Stokes photons. Since the photons in the second peak are indistinguishable, the coincidence count rate can be written as $P_{A^iB^j} = \frac{1}{2} + \frac{1}{2}ijV \cos(\alpha' + \beta')$, where i and $j = \pm 1$, and V is the visibility of the interference fringes. And the correlation coefficient E is inferred by the probability as

$$\begin{aligned} E(\alpha', \beta') = & \left(\sum_{ij} ij P_{A^iB^j} \right) / \left(\sum_{ij} P_{A^iB^j} \right) \\ = & V \cos(\alpha' + \beta'), \end{aligned} \quad (\text{F6})$$

The Clauser-Horne-Shimony-Holt (CHSH) Bell inequality gives

$$S = |E(\alpha, \beta) + E(\alpha', \beta) + E(\alpha, \beta') - E(\alpha', \beta')| \leq 2. \quad (\text{F7})$$

Therefore, making use of Eq. (F7), the parameter S has a maximum value of $S = 2\sqrt{2}V$ with $\alpha = 0^\circ$, $\alpha' = 90^\circ$, $\beta = 45^\circ$, and $\beta' = -45^\circ$. Thus, $V \geq 1/\sqrt{2}$ enables a violation of the CHSH Bell inequality.

APPENDIX G: EFFECT OF PUMP 2

Pump 2 is the key part of our entanglement construction. There are two main functions.

First, the retrieval efficiency of quantum memory cannot be 100%. Thus, if we remove pump 2, there will be such a situation: a write W_E pulse creates a collective single atom excitation, but the read pulse R_E does not read out an anti-Stokes photon AS_E ; however, the pulse R_L reads out an anti-Stokes photon AS_L . This situation will seriously affect our entanglement analysis. To avoid this detrimental effect, we added pump 2 in our work and the function of pump 2 has been proved by the coincidence count $N_{S_E-AS_L}$, shown as the dark blue circle in Fig. 3(b). The number of the coincidence count $N_{S_E-AS_E}$ is 6166. As the power of pump 2 is zero, the number of the coincidence count $N_{S_E-AS_L}$ is 4548, about 73.75% of the coincidence count $N_{S_E-AS_E}$. While as the power of pump 2 is 292.8 pJ, the number of the coincidence count $N_{S_E-AS_L}$ is 270, only about 4.38% of the coincidence count $N_{S_E-AS_E}$.

Second, if the pulse R_E does not retrieve the collective excitation state, the atomic spin wave will act like an input Stokes field to enhance the output Stokes photon number N_{S_L} [53], which is generated by the pulse W_L . This effect will make the number of photons generated by two time bins unequal.

Thus, we proposed the dual-addressing scheme to avoid the aforementioned problems, with the key function of pump 2 being to make the independence between two time bins.

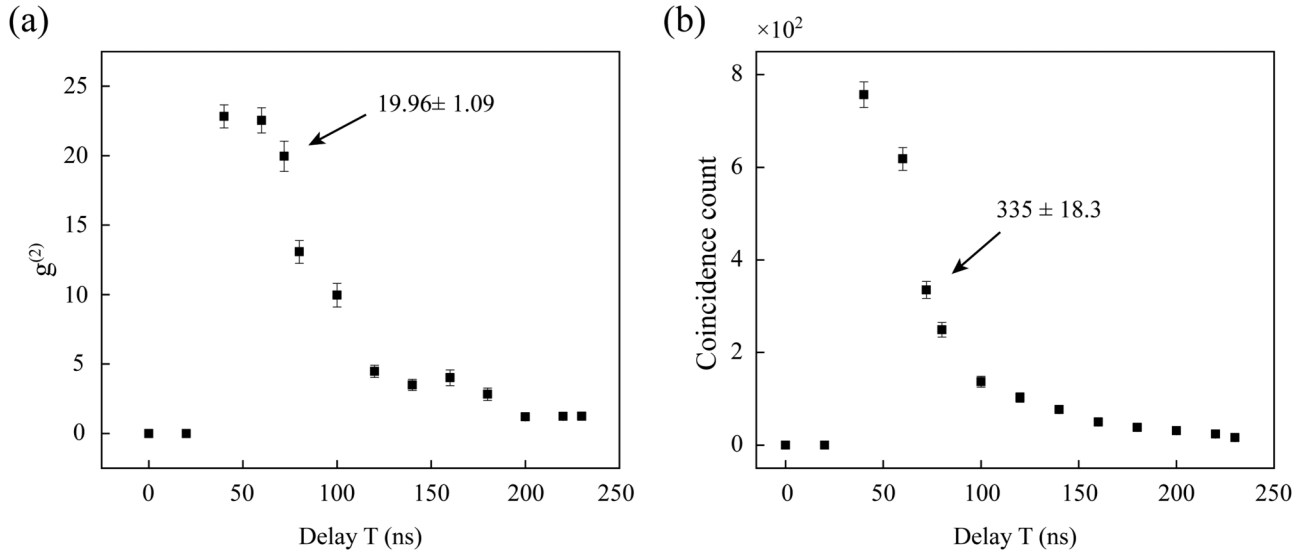


FIG. 9. Influence of after pulse. (a) The autocorrelation varies as a function of the delay. (b) The coincidence count varies as a function of the delay. Error bars are given by Poissonian statistics.

However, the existence of pump 2 brings a random-phase fluctuation to the late process. In other words, the relative phase between photons generated by two processes is a random value. This is well proved by measuring the photon counts of two output ports. As shown by the conceptual graph in Fig. 1(c), the statistical average beam-splitting ratio between the output port B^+ and the output port B^- is a constant of 50:50, which means the existence of a variable phase difference. The experimental result is shown in Fig. 8.

When there is no pump 2, the phase of the atomic spin wave changes continuously with time, and since the phase between the atomic spin wave and the Stokes field is anticorrelation, like the formula shown in Eq. (E14), the relative phase between photons generated by two processes is a constant. Therefore, we can obtain a sine curve of photon counts by scanning the phase of the interferometer, like the data shown in Fig. 8(a). While if the relative phase between photons generated by two processes is a random value, we can only obtain a straight line of photon counts by scanning the phase of the interferometer, like the data shown in Fig. 8(b).

APPENDIX H: INFLUENCE OF AFTER PULSE

In our work, we use the single-photon detector based on avalanche amplification, which has a fixed dead time and an after pulse effect.

When the single-photon detector receives a single photon, carriers appear in the gain medium and an avalanche occurs. The number of carriers increases rapidly and the detector outputs a signal. In a period of time after the avalanche process, the single-photon detector is turned off, which is called dead time (see the initial data shown in Fig. 9). After the dead time, the singlephoton detector turns on again for the next detection.

While a large number of carriers produced by the avalanche process cannot be completely eliminated. There are always some carriers stored in the semiconductor medium. Moreover, the storage time of some carriers can be much longer than the dead time. After the single-photon detector is turned on again, these stored carriers will be released in an uncertain time, and then avalanche amplification and the output electric signal occur. This electrical signal is the after pulse. Thus, the correlation between the after pulse and the signal photon is not

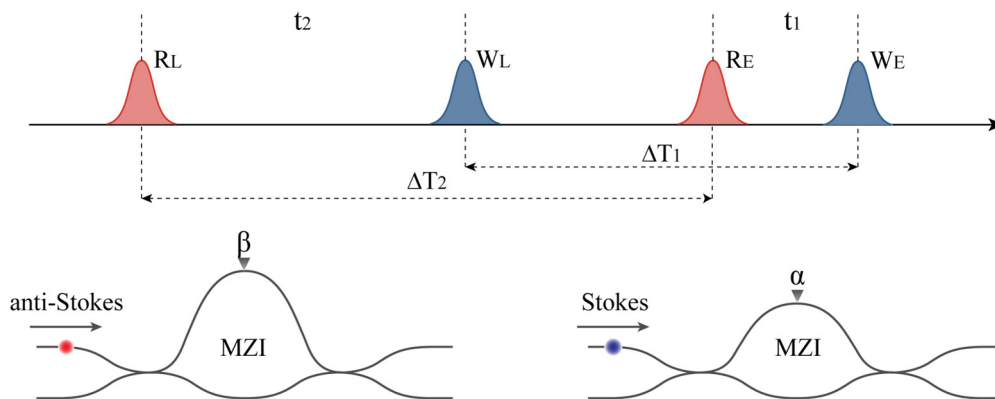


FIG. 10. Schematic of the unique features of the time-bin entanglement scheme.

the experimental result we want. So we can measure the after pulse effect by scanning the delay, as the data show in Fig. 9.

With the delay $T = 72$ ns, we have the autocorrelation $g^{(2)} = 19.96 \pm 1.09$ and the coincidence count $n = 335 \pm 18.3$, while the autocorrelation of the Stokes photons is $g_{S_E-S_L}^{(2)} = 1.15 \pm 0.03$ and the coincidence count is $N_{S_E-S_L} = 1836 \pm 42.8$. According to the coincidence count, the after pulse effect has 18.2% weight in our experimental results.

APPENDIX I: UNIQUE FEATURES OF THE TIME-BIN ENTANGLEMENT SCHEME

As for the entanglement scheme itself, the time sequences of each pulse can be adjusted flexibly. As shown in Fig. 10, for any entanglement analysis device (MZI), we can adjust

the time interval (ΔT_1 and ΔT_2) precisely to match the device, and in some experimental needs, which have different requirements for the unequal arm of the interferometer, we can adjust the time interval (ΔT_1 or ΔT_2) separately to match each device. The storage time of our scheme is not fixed. Under the condition of keeping the time interval (ΔT_2) unchanged, we can adjust the time interval (t_1) to change the storage time. Thus, we are able to build a time-bin entanglement embedded in quantum memory being flexibly compatible with different analysis devices.

In addition, it is possible to introduce the heralding property to our scheme by adding a magnetic field, which can induce a periodic dephasing and rephasing of the atomic excitation [21].

-
- [1] N. Gisin and R. Thew, Quantum communication, *Nat. Photonics* **1**, 165 (2007).
- [2] P. Zoller, Th. Beth, D. Binosi, R. Blatt, H. Briegel, D. Bruss, T. Calarco, J. I. Cirac, D. Deutsch, J. Eisert, A. Ekert, C. Fabre, N. Gisin, P. Grangiere, M. Grassl, S. Haroche, A. Imamoglu, A. Karlson, J. Kempe, L. Kouwenhoven, S. Kröll *et al.* Quantum information processing and communication, *Eur. Phys. J. D* **36**, 203 (2005).
- [3] C. H. Bennett, G. Brassard, C. Crépeau, R. Jozsa, A. Peres, and W. K. Wootters, Teleporting an Unknown Quantum State via Dual Classical and Einstein-Podolsky-Rosen Channels, *Phys. Rev. Lett.* **70**, 1895 (1993).
- [4] N. Sangouard, C. Simon, H. de Riedmatten, and N. Gisin, Quantum repeaters based on atomic ensembles and linear optics, *Rev. Mod. Phys.* **83**, 33 (2011).
- [5] A. I. Lvovsky, B. C. Sanders, and W. Tittel, Optical quantum memory, *Nat. Photonics* **3**, 706 (2009).
- [6] A. Ekert, Quantum Cryptography Based on Bell's Theorem, *Phys. Rev. Lett.* **67**, 661 (1991).
- [7] A. Steane, Quantum computing, *Rep. Prog. Phys.* **61**, 117 (1998).
- [8] B. B. Blinov, D. L. Moehring, L.-M. Duan, and C. Monroe, Observation of entanglement between a single trapped atom and a single photon, *Nature (London)* **428**, 153 (2004).
- [9] J. Hofmann, M. Krug, N. Ortegel, L. Gérard, M. Weber, W. Rosenfeld, and H. Weinfurter, Heralded entanglement between widely separated atoms, *Science* **337**, 72 (2012).
- [10] J. Brendel, N. Gisin, W. Tittel, and H. Zbinden, Pulsed Energy-Time Entangled Twin-Photon Source for Quantum Communication, *Phys. Rev. Lett.* **82**, 2594 (1999).
- [11] K. S. Choi, H. Deng, J. Laurat, and H. J. Kimble, Mapping photonic entanglement into and out of a quantum memory, *Nature (London)* **452**, 67 (2008).
- [12] L. Allen, M. W. Beijersbergen, R. J. C. Spreeuw, and J. P. Woerdman, Orbital angular momentum of light and the transformation of Laguerre-Gaussian laser modes, *Phys. Rev. A* **45**, 8185 (1992).
- [13] Y. Chen, J. Gao, Z.-Q. Jiao, K. Sun, W.-G. Shen, L.-F. Qiao, H. Tang, X.-F. Lin, and X.-M. Jin, Mapping Twisted Light into and out of a Photonic Chip, *Phys. Rev. Lett.* **121**, 233602 (2018).
- [14] I. Marcikic, H. de Riedmatten, W. Tittel, H. Zbinden, M. Legré, and N. Gisin, Distribution of Time-Bin Entangled Qubits over 50 km of Optical Fiber, *Phys. Rev. Lett.* **93**, 180502 (2004).
- [15] T. Inagaki, N. Matsuda, O. Tadanaga, M. Asobe, and H. Takesue, Entanglement distribution over 300 km of fiber, *Opt. Express* **21**, 23241 (2013).
- [16] Y. Yu, F. Ma, X.-Y. Luo, B. Jing, P.-F. Sun, R.-Z. Fang, C.-W. Yang, H. Liu, M.-Y. Zheng, X.-P. Xie, W.-J. Zhang, L.-X. You, Z. Wang, T.-Y. Chen, Q. Zhang, X.-H. Bao, and J.-W. Pan, Entanglement of two quantum memories via fibres over dozens of kilometres, *Nature (London)* **578**, 240 (2020).
- [17] H. Takesue, Long-distance distribution of time-bin entanglement generated in a cooled fiber, *Opt. Express* **14**, 3453 (2006).
- [18] B. Hensen, H. Bernien, A. E. Dreau, A. Reiserer, N. Kalb, M. S. Blok, J. Ruitenberg, R. F. L. Vermeulen, R. N. Schouten, C. Abellan, W. Amaya, V. Pruneri, M. W. Mitchell, M. Markham, D. J. Twitchen, D. Elkouss, S. Wehner, T. H. Taminiau, and R. Hanson, Loophole-free Bell inequality violation using electron spins separated by 1.3 kilometres, *Nature (London)* **526**, 682 (2015).
- [19] K. De Greve, L. Yu, P. L. McMahon, J. S. Pelc, C. M. Natarajan, N. Y. Kim, E. Abe, S. Maier, C. Schneider, M. Kamp, S. Hofling, R. H. Hadfield, A. Forchel, M. M. Fejer, and Y. Yamamoto, Quantum-dot spin-photon entanglement via frequency downconversion to telecom wavelength, *Nature (London)* **491**, 421 (2012).
- [20] H. Jayakumar, A. Predojević, T. Kauten, T. Huber, G. S. Solomon, and G. Weihs, Time-bin entangled photons from a quantum dot, *Nat. Commun.* **5**, 4251 (2014).
- [21] P. Farrera, G. Heinze, and H. de Riedmatten, Entanglement between a Photonic Time-Bin Qubit and a Collective Atomic Spin Excitation, *Phys. Rev. Lett.* **120**, 100501 (2018).
- [22] K. Kutluer, E. Distante, B. Casabone, S. Duranti, M. Mazzer, and H. de Riedmatten, Time Entanglement between a Photon and a Spin Wave in a Multimode Solid-State Quantum Memory, *Phys. Rev. Lett.* **123**, 030501 (2019).
- [23] H.-J. Briegel, W. Dür, J. I. Cirac, and P. Zoller, Quantum Repeaters: The Role of Imperfect Local Operations in Quantum Communication, *Phys. Rev. Lett.* **81**, 5932 (1998).
- [24] L.-M. Duan, M. D. Lukin, J. I. Cirac, and P. Zoller, Long-distance quantum communication with atomic

- ensembles and linear optics, *Nature (London)* **414**, 413 (2001).
- [25] S. E. Harris, J. E. Field, and A. Imamoglu, Nonlinear Optical Processes Using Electromagnetically Induced Transparency, *Phys. Rev. Lett.* **64**, 1107 (1990).
- [26] M. D. Eisaman, A. André, F. Massou, M. Fleischhauer, A. S. Zibrov, and M. D. Lukin, Electromagnetically induced transparency with tunable single-photon pulses, *Nature (London)* **438**, 837 (2005).
- [27] H. Zhang, X.-M. Jin, J. Yang, H.-N. Dai, S.-J. Yang, T.-M. Zhao, J. Rui, Y. He, X. Jiang, F. Yang, G.-S. Pan, Z.-S. Yuan, Y. Deng, Z.-B. Chen, X.-H. Bao, S. Chen, B. Zhao, and J.-W. Pan, Preparation and storage of frequency-uncorrelated entangled photons from cavity-enhanced spontaneous parametric down-conversion, *Nat. Photonics* **5**, 628 (2011).
- [28] B. Julsgaard, A. Kozhekin, and E. S. Polzik, Experimental long-lived entanglement of two macroscopic objects, *Nature (London)* **413**, 400 (2001).
- [29] B. Julsgaard, J. Sherson, J. I. Cirac, J. Fiurášek, and E. S. Polzik, Experimental demonstration of quantum memory for light, *Nature (London)* **432**, 482 (2004).
- [30] S. A. Moiseev and S. Kröll, Complete Reconstruction of the Quantum State of a Single-Photon Wave Packet Absorbed by a Doppler-Broadened Transition, *Phys. Rev. Lett.* **87**, 173601 (2001).
- [31] B. Kraus, W. Tittel, N. Gisin, M. Nilsson, S. Kröll, and J. I. Cirac, Quantum memory for nonstationary light fields based on controlled reversible inhomogeneous broadening, *Phys. Rev. A* **73**, 020302(R) (2006).
- [32] M. Afzelius, C. Simon, H. de Riedmatten, and N. Gisin, Multimode quantum memory based on atomic frequency combs, *Phys. Rev. A* **79**, 052329 (2009).
- [33] B. C. Buchler, M. Hosseini, G. Hétet, B. M. Sparkes, and P. K. Lam, Precision spectral manipulation of optical pulses using a coherent photon echo memory, *Opt. Lett.* **35**, 1091 (2010).
- [34] M. Hosseini, B. M. Sparkes, G. Campbell, P. K. Lam, and B. C. Buchler, High efficiency coherent optical memory with warm rubidium vapour, *Nat. Commun.* **2**, 174 (2011).
- [35] K. F. Reim, J. Nunn, V. O. Lorenz, B. J. Sussman, K. C. Lee, N. K. Langford, D. Jaksch, and I. A. Walmsley, Towards high-speed optical quantum memories, *Nat. Photonics* **4**, 218 (2010).
- [36] K. F. Reim, J. Nunn, X.-M. Jin, P. S. Michelberger, T. F. M. Champion, D. G. England, K. C. Lee, W. S. Kolthammer, N. K. Langford, and I. A. Walmsley, Multipulse Addressing of a Raman Quantum Memory: Configurable Beam Splitting and Efficient Readout, *Phys. Rev. Lett.* **108**, 263602 (2012).
- [37] S. Manz, T. Fernholz, J. Schmiedmayer, and J.-W. Pan, Collisional decoherence during writing and reading quantum states, *Phys. Rev. A* **75**, 040101(R) (2007).
- [38] P. S. Michelberger, T. F. M. Champion, M. R. Sprague, K. T. Kaczmarek, M. Barbieri, X. M. Jin, D. G. England, W. S. Kolthammer, D. J. Saunders, J. Nunn, and I. A. Walmsley, Interfacing GHz-bandwidth heralded single photons with a warm vapour Raman memory, *New J. Phys.* **17**, 043006 (2015).
- [39] J.-P. Dou, A.-L. Yang, M.-Y. Du, D. Lao, H. Li, X.-L. Pang, J. Gao, L.-F. Qiao, H. Tang, and X.-M. Jin, Direct observation of broadband nonclassical states in a room-temperature light-matter interface, *npj Quantum Inf* **4**, 31 (2018).
- [40] X.-L. Pang, A.-L. Y. J.-P. Dou, H. Li, C.-N. Zhang, E. Poem, D. J. Saunders, H. Tang, J. Nunn, I. A. Walmsley, and X.-M. Jin, A Hybrid Quantum Memory Enabled Network at Room Temperature, *Sci. Adv.* **6**, eaax1425 (2020).
- [41] J. Nunn, Quantum memory in atomic ensembles. Ph.D. thesis, University of Oxford, 2008.
- [42] B. Zhao, Y.-A. Chen, X.-H. Bao, T. Strassel, C.-S. Chuu, X.-M. Jin, J. Schmiedmayer, Z.-S. Yuan, S. Chen, and J.-W. Pan, A millisecond quantum memory for scalable quantum networks, *Nat. Phys.* **5**, 95 (2009).
- [43] J.-P. Dou, A.-L. Yang, M.-Y. Du, D. Lao, J. Gao, L.-F. Qiao, H. Li, X.-L. Pang, Z. Feng, H. Tang, and X.-M. Jin, A broadband DLCZ quantum memory in room-temperature atoms, *Commun. Phys.* **1**, 55 (2018).
- [44] R. Loudon, *The Quantum Theory of Light*, 3rd ed. (Oxford University, Oxford, 2010).
- [45] J. F. Clauser, Experimental distinction between the quantum and classical field-theoretic predictions for the photoelectric effect, *Phys. Rev. D* **9**, 853 (1974).
- [46] J. D. Franson, Bell Inequality for Position and Time, *Phys. Rev. Lett.* **62**, 2205 (1989).
- [47] J. F. Clauser, M. A. Horne, A. Shimony, and R. A. Holt, Proposed Experiment to Test Local Hidden-Variable Theories, *Phys. Rev. Lett.* **23**, 880 (1969).
- [48] J. Huang and P. Kumar, Observation of Quantum Frequency Conversion, *Phys. Rev. Lett.* **68**, 2153 (1992).
- [49] M. A. Albota and F. N. C. Wong, Efficient single-photon counting at 1.55 μm by means of frequency upconversion, *Opt. Lett.* **29**, 1449 (2004).
- [50] S. Tanzilli, W. Tittel, M. Halder, O. Alibart, P. Baldi, N. Gisin, and H. Zbinden, A photonic quantum information interface, *Nature (London)* **437**, 116 (2005).
- [51] C.-L. Bian, L.-Q. Chen, G.-W. Zhang, Z. Y. Ou, and W. Zhang, Retrieval of phase memory in two independent atomic ensembles by Raman process, *Europhys. Lett.* **97**, 34005 (2012).
- [52] M. G. Raymer, Quantum state entanglement and readout of collective atomic-ensemble modes and optical wave packets by stimulated Raman scattering, *J. Mod. Opt.* **51**, 1739 (2004).
- [53] L. Q. Chen, G.-W. Zhang, C.-H. Yuan, J. Jing, Z. Y. Ou, and W. Zhang, Enhanced Raman scattering by spatially distributed atomic coherence, *Appl. Phys. Lett.* **95**, 041115 (2009).